



Measurement of turbulence energy dissipation rate by a standalone high-resolution Doppler lidar

Abdul Haseeb Syed¹, Jakob Mann¹, and Mohammadreza Manami^{1,2}

¹DTU Wind and Energy Systems, Roskilde, Denmark

²Lidar Division, Lumibird SA, Lannion, France

Correspondence: Jakob Mann (jmsq@dtu.dk)

Abstract. A second-order structure function model for the lidar line of sight (LOS) velocities is proposed. This structure function model corrects for the turbulence filtering due to the probe volume averaging effect using a Gaussian weighting function. It takes advantage of the high range gate resolution of the BEAM 6x pulsed lidar used in this study, i.e., 3m, to effectively resolve the inertial subrange. The structure function model is then used to obtain the turbulence energy dissipation rate (ε) by fitting the model over lidar measurements in the inertial subrange. Unlike previously presented structure function methods to evaluate ε in the literature, this method has a weaker dependence on the turbulence length scale. The estimated ε values obtained from the lidar are compared with the values obtained from ultrasonic anemometers at three heights: 103 m, 175 m, and 241 m. The comparison results show excellent correlation between the two sets, with a Pearson correlation coefficient (ρ) value of more than 0.9 at all three heights. The observed bias was also found to be very small, i.e., more than 50% of all the lidar-measured ε values were found within $\pm 20\%$ of the sonic-measured values. This method relies on the proper detection of the inertial subrange; hence, during very stable atmospheric conditions, the model fitting on the measurements produced relatively larger errors, due to the difficulty in detecting the inertial subrange. Applications of this method include, but are not limited to, quantifying turbulence in the wake of aircraft, understanding pollutant dispersion in urban environments, and wind resource and turbulence assessment in areas where erecting a meteorological mast is not possible.

15 1 Introduction

Turbulence measurements hold paramount significance in atmospheric sciences and renewable energy applications. These measurements are used to understand and quantify aerosols, heat, moisture, and momentum in the atmospheric boundary layer (Stull, 1988). In the troposphere, turbulence governs energy and momentum exchange between the Earth's surface and the air above it. Turbulence measurements are also used to monitor and understand air quality, pollutant dispersion, and heat dynamics in urban meteorology. Atmospheric turbulence is usually measured with *in situ* instruments such as a hot-wire anemometer or a sonic anemometer that can be installed on a meteorological mast. These instruments measure turbulence at a fixed point in space. Erecting a meteorological mast for turbulence measurements may not always be feasible, especially in complex terrain, deep offshore seas, or in conditions where *in situ* measurements are not possible, e.g., aircraft wake vortices. In such cases, remote sensing devices like Doppler wind lidars can be employed to estimate atmospheric turbulence remotely. Commercial



40

55



scanning lidars also provide the capability to get multi-point statistics and vertical profiles, thus presenting a more detailed view of the atmosphere.

Estimating turbulence from a Doppler wind lidar is not a novel concept. There are two key challenges associated with it, as delineated by Peña et al. (2025): turbulence contamination and probe-volume averaging. The former arises from the reconstruction of wind velocity components from lidar line-of-sight (LOS) velocities, while the latter is inherent to the measuring principle of Doppler lidars, as lidars do not record point measurements; rather, they measure within a probe volume, acting as a turbulence filter. A number of methods and scanning strategies have been proposed to operate Doppler lidars as a standalone instrument to measure atmospheric turbulence. Eberhard et al. (1989) used a short-pulse Doppler wind lidar with a range gate resolution of 150 m to measure Reynolds stresses and turbulence kinetic energy (TKE) profiles in the atmosphere. Their method relies on the conical scanning of the atmosphere at a fixed elevation angle and deducing Reynolds stress values directly from the individual beam LOS variances. This approach avoids the cross-contamination between the wind field components; however, it does not address the issue of turbulence filtering due to the probe volume averaging (Bonin et al., 2017; Sathe and Mann, 2013). This method has been further improved and optimized for a Doppler beam swing (DBS) scanning pattern, where only five azimuth measurements at a fixed elevation angle and one vertical measurement are obtained to deduce the full Reynolds stress tensor (Sathe et al., 2015).

A significant amount of research efforts has been made to address the turbulence filtering or the attenuation of small-scale turbulence due to probe-volume averaging. Frehlich et al. (1998), and Frehlich and Cornman (2002) utilized the LOS velocity structure function (D(r)), where r is the separation distance) for a pulsed lidar to estimate the turbulence energy dissipation rate ε . They removed the effect of spatial averaging using theoretical corrections, such as modeling the lidar range weighting as a Gaussian function. In this approach, the measured second-order structure function is fitted to a theoretical D(r) model that accounts for the probe-volume averaging of the lidar LOS velocities. Smalikho et al. (2005) obtained ε from the longitudinal structure function of LOS velocities measured by a 2 μ m lidar with a range gate resolution of 30 m and compared it with the ε estimates obtained from the Doppler spectrum width (DSW) method, confirming the results with numerical simulations. Their results showed a high correlation between the two methods, and a reduction in bias was observed as ε became higher. Smalikho and Banakh (2017) and Wildmann et al. (2020) utilized the azimuthal structure function of LOS velocities obtained from the conically scanning vertical profiling lidars to estimate ε and TKE. Both studies account for the probe volume averaging by defining a transverse filter function. However, the latter introduced an additional advection filter to account for the advection of turbulence within the scanning plane. The ε estimates were then compared with the sonic anemometers. Correcting for advection did reduce the bias; however, the random error, as indicated by the observed scatter, was still found to be relatively high.

A major drawback of these methods is that the presented D(r) models are also dependent on the outer scale of turbulence \mathcal{L}_o . To obtain \mathcal{L}_o , it was often assumed that the large-scale turbulence is isotropic and can be modeled by an isotropic spectral model, such as the von Kármán spectral model. However, the von Kármán spectral model can only be used for special cases involving isotropic and homogeneous turbulence. In reality, the atmospheric turbulence is highly anisotropic (Mann, 1994; Kaimal and Finnigan, 1994). In order to find ε from such methods, the modeled D(r) was fitted to the measurements in





such a way that the best fitting takes place for both variables: ε and \mathcal{L}_o (Frehlich and Cornman, 2002; Frehlich et al., 1998; Smalikho et al., 2005). The best fit obtained using this method may not provide the best ε value, since \mathcal{L}_o is also being fitted to minimize the error function. Any anisotropy in the large-scale turbulence would distort ε estimates. Furthermore, it unnecessarily complicates the fitting procedure as more than one variable is involved.

Turbulence energy dissipation rate can also be obtained through the one-dimensional LOS velocity spectrum, provided that the inertial sub-range is detected (Davis et al., 2008; O'Connor et al., 2010; Bodini et al., 2018; Wildmann et al., 2019). However, this method requires invoking Taylor's hypothesis of frozen turbulence (Taylor, 1935) and a suitable choice of \mathcal{L}_o . The effect of turbulence filtering due to probe volume averaging was also modeled to get the corrected velocity spectrum, which improved the prediction of ε (Banakh and Smalikho, 1997; Drobinski et al., 2000). In summary, there are two primary ways of estimating ε from the Doppler lidar measurements reported in the scientific literature: the structure function method and the velocity spectrum method. Both these methods usually require knowledge about the outer scale of turbulence, \mathcal{L}_o , and may invoke the assumption of frozen turbulence.

In this article, we present an improved second-order longitudinal structure function model for lidar LOS velocities, which also accounts for the probe volume averaging in a pulsed lidar. The presented structure function model improves on the previously described methods in the following two ways: (i) the lidar system used in this study has a very high resolution of range gates along the beam, i.e., 3 m, which offers an enhanced detection of the inertial subrange and (ii) the use of longitudinal D(r) means that there is no need to assume Taylor's frozen turbulence hypothesis, as all the LOS measurements along the lidar beam are made at the same instant with a constant separation distance r between the range gates. This ensures that the structure function model only depends on ε in the inertial subrange. The model is then used to estimate the turbulence energy dissipation rate ε in the atmospheric boundary layer, and the values are validated against sonic anemometer measurements at three heights of 103 m, 175 m, and 241 m above ground level at a test site in Denmark.

The second-order longitudinal structure function model for lidar LOS velocities is presented in detail in Section 2. In Section 3, the test site and information about the lidar and the validation data (ultrasonic anemometers) are provided. Section 4 entails the complete workflow for estimating ε from the ultrasonic anemometers and the lidar data. Section 5 describes the validation of lidar-derived ε estimates with the sonic anemometers' data, and the relevant discussion. Section 6 concludes the article with the description of the salient features of the model and a summary of the significant results from this study.

2 Second-order structure function model for lidar line of sight velocities

The second-order velocity structure function is the variance of the difference in velocity between two points x and x+r, where r is the separation vector between them. The second-order structure function can be defined as:

$$D(r) = \langle [\boldsymbol{n} \cdot \boldsymbol{v}(\boldsymbol{x}) - \boldsymbol{n} \cdot \boldsymbol{v}(\boldsymbol{x} + \boldsymbol{r})]^2 \rangle , \qquad (1)$$

where n = r/|r|. Since the component $n \cdot v$ of the velocity vector is aligned with n, this is called a longitudinal structure function. Kolmogorov (Pope, 2000) hypothesized that in the inertial subrange, the turbulence is locally isotropic and D(r) is





only a function of the turbulent energy dissipation rate ε , the separation distance r, and the universal Kolmogorov constant $C_K \approx 2$. Hence, for $|r| \ll \mathcal{L}_o$, where \mathcal{L}_o is the integral length scale or the size of the largest eddies,

$$D(r) = C_K(\varepsilon r)^{2/3} . (2)$$

95 The lidar used in this study measures filtered line-of-sight velocities at several range gates along the beam. A lidar does not make point measurements but rather senses the LOS wind distribution in a weighted sample volume in the form of a Doppler spectrum. Different methods are used by lidar manufacturers to estimate the representative wind speed from the Doppler spectrum. Following Held and Mann (2018), if we assume that the effect of probe volume on turbulence attenuation can be modeled by the centroid method of determining the dominant frequency in the Doppler spectrum, then the line-of-sight velocity of the lidar beam can be defined as:

$$v_r(\mathbf{x}) = \int_{-\infty}^{\infty} \varphi(s) \, \mathbf{n} \cdot \mathbf{v}(s\mathbf{n} + \mathbf{x}) \, ds \quad , \tag{3}$$

where n is a unit vector along the beam direction, x is the center of the lidar measuring volume at the point of interest, and s is the distance along the beam from the point x. $\varphi(s)$ is the weighting function normalized to unit integral, and a Gaussian shape is assumed here:

105
$$\varphi(s) = \frac{1}{\sigma\sqrt{2\pi}}e^{-\frac{s^2}{2\sigma^2}}$$
, (4)

where σ is the standard deviation of the Gaussian distribution. Though Held and Mann (2018) defined (3) for a continuous-wave lidar system, the same can be assumed for a pulsed lidar system. Dolfi-Bouteyre et al. (2017) evaluated the accuracy of the centroid frequency estimator method with a coherent pulsed lidar system and found it to perform well in calculating both the first- and second-order moments of the Doppler spectrum. The longitudinal structure function along the beam then becomes:

$$D_{\text{lidar}}(r) = \left\langle \left[\int_{-\infty}^{\infty} \left\{ v(x+s) - v(x+r+s) \right\} \varphi(s) ds \right]^2 \right\rangle , \qquad (5)$$

where r is the distance between two range gates along the beam and $v = n \cdot v$ is the velocity component along the beam direction as a function of distance along the beam. It is assumed that r and σ are small as compared to the turbulence length scale \mathcal{L}_o and the flow is homogeneous. This can be solved for the inertial subrange as (see Appendix A for a detailed derivation):

115
$$D_{\text{lidar}}(r) = \frac{C_K}{\sqrt{\pi}} 2^{2/3} \sigma^{2/3} \varepsilon^{2/3} \Gamma\left(\frac{5}{6}\right) \left\{ {}_1F_1\left[-\frac{1}{3}, \frac{1}{2}, -\frac{r^2}{4\sigma^2}\right] - 1 \right\},$$
 (6)

where Γ is the Gamma function, and ${}_1F_1$ is the confluent hypergeometric function. Here we note that the lidar structure function also depends on the standard deviation of the Gaussian weighting function σ . The main assumption for accurately estimating ε is that σ should be less than \mathcal{L}_o . If there is less turbulence in the atmosphere and the length scale of the turbulence is smaller than the sampling volume of the lidar, then the turbulence fluctuations will be filtered out. The choice of σ depends on the





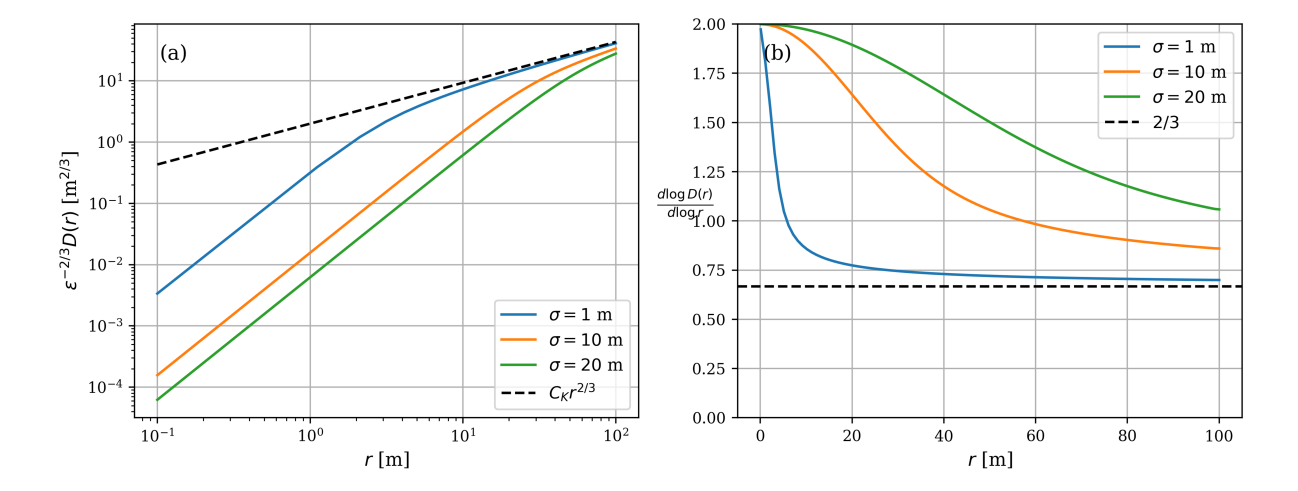


Figure 1. (a) Normalized structure function $\varepsilon^{-2/3}D(r)$ as a function of the separation distance r for three different values of σ : 1 m, 10 m, and 20 m. A $C_K r^{2/3}$ reference line is also added. (b) $d \log D(r)/d \log r$ as a function of r. The dashed black line represents a slope value of 2/3.

lidar instrument and can be obtained by fitting the data for a range of σ values and then selecting a value that provides the least amount of bias against true values. Figure 1(a) describes how D_{lidar} changes as a function of r for three different σ values. The change in local slope of the structure function is also a function of r, as seen in Fig. 1(b). Given the measured structure function from a high-resolution lidar beam, Eq. 6 can be fitted using the least squares method or other optimization techniques to obtain the turbulence energy dissipation rate ε .

3 Data and site description

3.1 Test site

125

130

135

The Østerild test site is located in the northern region of Jutland, Denmark, situated between Limfjorden and Skagerrak, as shown in the inset of Figure 2. As of 2024, the site hosts nine wind turbines for testing purposes, arranged in a north-south orientation, spanning approximately 4.7 km. Figure 2 illustrates the positions of these turbines, denoted by red dots. Each turbine is accompanied by a mast positioned approximately 2.5–4 rotor diameters to the west, with heights corresponding to the hub height of the turbines. Additionally, two light masts are positioned to the north and south of the turbine row (the north mast, which is relevant for this study, is marked by a yellow dot in Figure 2). The terrain depicted in Figure 2 features both flat and heterogeneous characteristics, comprising a mosaic of crop and agricultural lands, urban settlements, and forested areas. Further detailed information about the Østerild site can be found in Peña (2019). For the present study, we focus only on the North mast, which is a 250 m tall mast with a triangular lattice structure. The mast is equipped with cup and ultrasonic





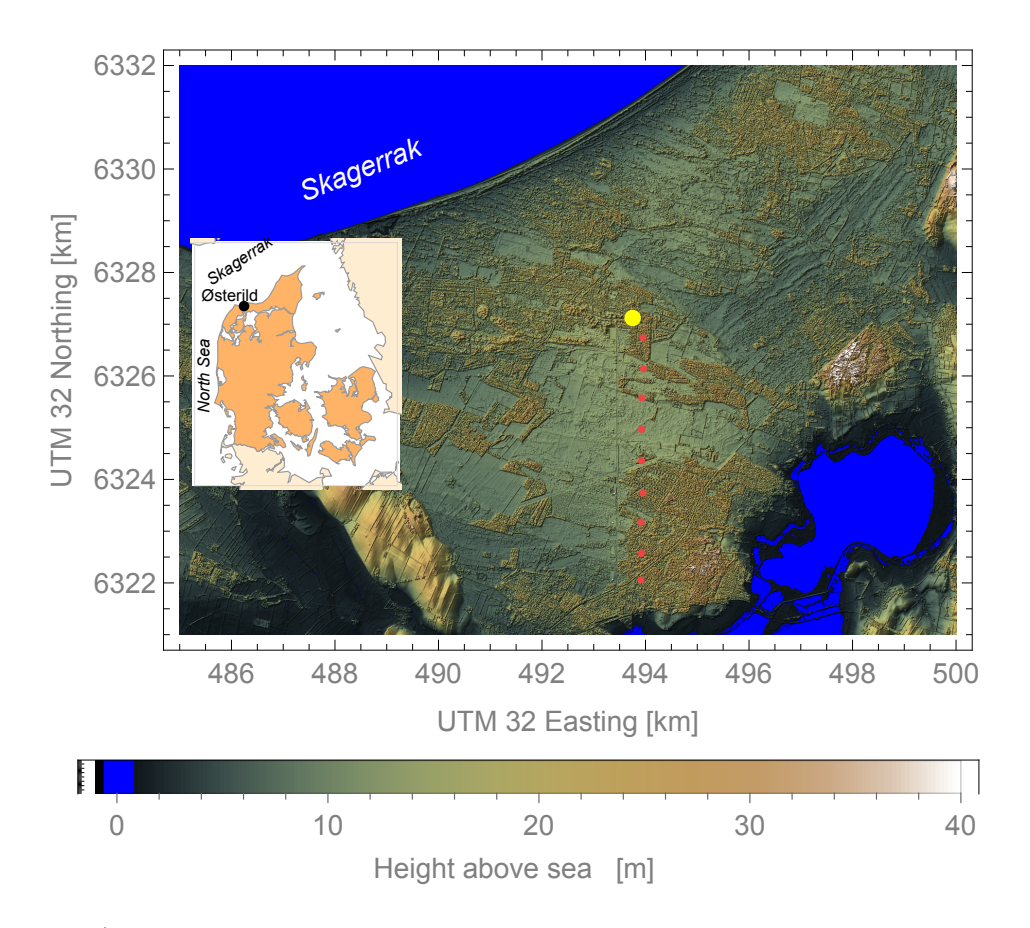


Figure 2. Position of the Østerild site in Denmark (inset) and a digital surface model of the surrounding area. The 250 m mast is in yellow, while the turbine stands at the test site around the red dots. It is seen that the area is relatively flat and there is low forest to the north west of the mast. The forest to the west of the turbine row has been cleared out to almost 2 km.

anemometers mounted on the booms oriented at 0° from the north. The lidar pad is about 10 m west of the mast and contains the vertical profiling BEAM 6x lidar. The details about the lidar and sonic data are as follows.

3.2 BEAM 6x lidar

140

The *Halo Photonics by Lumibird BEAM 6x Wind Sciences* pulsed lidar is used in this study because of its high-resolution of range gates along the beam. The lidar has six beams, where five inclined beams with an elevation angle of about 60° are arranged in a pentagon pattern, i.e., with an azimuthal separation of 72°. The sixth beam is the vertical beam staring into zenith, directly measuring vertical velocities. A schematic of the lidar beams is displayed in Fig. 3. The lidar can measure radial velocities up to 1000 m, with the range gates separated by 3 m along the beam, which is an important quality of the instrument for the structure function estimation. The lidar was placed alongside the mast from 09 April 2024 to 06 December 2024. The lidar measures LOS velocities along a single beam in approximately 1 second, so one complete Doppler Beam





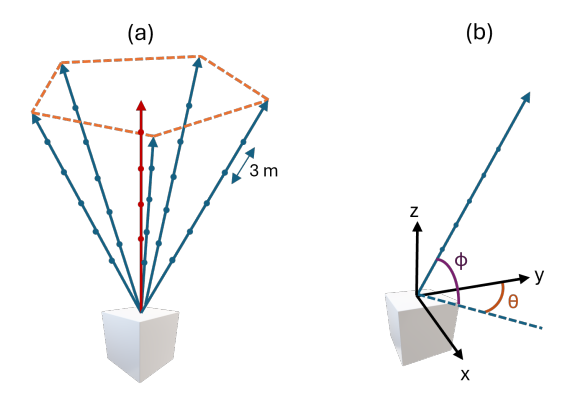


Figure 3. (a) A schematic diagram showing the lidar beams' orientation and the distribution of range gates along the beams. The red arrow depicts the vertical beam. (b) The coordinate system used for the beams. Here θ represents the azimuth angle, and ϕ represents the elevation angle from the ground.

Swing (DBS) scan takes \sim 6 seconds. The lidar data availability is determined by the *Intensity* parameter, which is an indicator of the signal-to-noise ratio. An *Intensity* threshold value of 1.015 is used to filter out the noise from the signal, following the manufacturer's recommendation.

3.3 Ultrasonic anemometers

The mast has Metek USA-1 Scientific ultrasonic anemometers at elevations of 37 m, 103 m, 175 m, and 241 m. The anemometers are configured with a sampling frequency of 20 Hz. We convert the x, y, z speed components in the sonic output from a Cartesian coordinate system to the longitudinal u, transverse v, and vertical w wind speed components. Afterward, we align the u component with the mean wind direction observed during each 10 minutes. Some peaks/outliers were observed in the sonic data, which were removed using a Hampel filter (Liu et al., 2004) with a window size of five measurement points and an outlier threshold of three standard deviations. The ultrasonic anemometer data at 37 m is used to classify the data into different atmospheric stability classes by using the Monin-Obukhov length:

$$L_o = -\frac{u_*^3}{\kappa(g/T)\overline{w'\Theta_v'}} \quad , \tag{7}$$

where u_* is the frictional velocity, κ is the von Kármán constant, g is the gravitational acceleration, T is the reference temperature, and $\overline{w'\Theta'_v}$ is the virtual kinematic heat flux where Θ_v is the virtual potential temperature. Table 1 describes seven different stability classes from "Very Unstable" to "Very Stable" based on Monin-Obukhov length L_o .

4 Workflow for estimating ε

In order to estimate the turbulent energy dissipation rate ε , the primary challenge is the detection of the inertial subrange. This can be done in several ways: either through the power spectral density of the wind components or by using the structure function





Table 1. Stability classification based on the Monin-Obukhov length

Obukhov Length L_o [m]	Atmospheric Stability
$-100 < L_o \le -50$	Very Unstable (vu)
$-200 < L_o \le -100$	Unstable (u)
$-500 < L_o \le -200$	Near-Neutral Unstable (nnu)
$ L_o \ge 500$	Neutral (n)
$200 \le L_o < 500$	Near-Neutral Stable (nns)
$50 \le L_o < 200$	Stable (s)
$10 \le L_o < 50$	Very Stable (vs)

method. For sonic anemometers, the straightforward way is to plot a wavenumber spectrum of the u, v, or w wind component by assuming Taylor's frozen turbulence hypothesis. In the inertial subrange, the one-point, two-sided velocity spectra in terms of wavenumber k_1 (where $k_1 = 2\pi f/\overline{U}$; f is the sampling frequency and \overline{U} is the mean wind speed) are given by:

$$F_u(k_1) = \frac{9}{55} \alpha \varepsilon^{2/3} k_1^{-5/3} , \qquad (8)$$

and

180

$$F_v(k_1) = F_w(k_1) = \frac{12}{55} \alpha \varepsilon^{2/3} k_1^{-5/3} , \qquad (9)$$

where α is the spectral Kolmogorov constant with a value of ~ 1.5 (Pope, 2000). To detect the inertial subrange, a compensated spectrum $k_1^{5/3} \cdot F_u(k_1)$ is plotted against k_1 . The region where $d(k_1^{5/3} \cdot F_u(k_1))/dk_1 \approx 0$ represents the inertial subrange (Peña et al., 2019; Syed et al., 2023). Here, we only used wavenumber in the range 5×10^{-2} m⁻¹ < $k_1 < 10^0$ m⁻¹ to detect the inertial subrange and allowed a slope deviation of only 10%. After detecting the range, $\varepsilon_{\text{sonic}}$ is calculated using:

$$\varepsilon_{\text{sonic}} = \left[\frac{55}{9\alpha} \, \overline{k_1^{5/3} \cdot F_u(k_1)} \right]^{3/2},\tag{10}$$

175 where represents the mean value in the inertial subrange.

For the $\varepsilon_{\text{lidar}}$ calculation from the BEAM 6x lidar, the structure function approach is adopted. The benefit of such an approach is that since lidar beams measure LOS velocities at range gates physically separated by a distance at the same time, there is no need to assume Taylor's frozen turbulence hypothesis. The distance between the range gates is constant, i.e., 3 m. Furthermore, assuming that the sampling volume $\sigma < \mathcal{L}_o$, it would allow resolving the ε without \mathcal{L}_o dependence. The following steps are taken to derive $\varepsilon_{\text{lidar}}$ from a single 10-minute period from lidar LOS data:

1. For a selected height h, range gates within $h\pm 12$ m are selected to get the measured longitudinal structure function from LOS velocities. For each beam, a mean structure function is obtained for all the scans in the 10-minute time period.



190

210



2. Another average from all six beams is taken to obtain the mean longitudinal structure function, $D_{\rm meas}$. The lidar structure function model described in Eq. 6 is fitted to the inertial subrange of the mean measured structure function for r < 24 m using the least squares fitting method to obtain $\varepsilon_{\rm lidar}$. The downhill simplex algorithm is used to minimize the fitting error function, described as:

$$\sum_{j=1}^{N} [\log_{10} D_{\text{lidar}}(r_j, \varepsilon, \sigma) - \log_{10} D_{\text{meas}}(r_j)]^2$$
(11)

3. The lidar data is then classified into two different categories based on the percentage error obtained from the model fitting, defined as:

$$\%Error = (10^{RMSE} - 1) \times 100 , \qquad (12)$$

where,

$$RMSE = \sqrt{\frac{\sum_{j=1}^{N} [\log_{10} D_{\text{lidar}}(r_j, \varepsilon, \sigma) - \log_{10} D_{\text{meas}}(r_j)]^2}{N}} \quad . \tag{13}$$

The first is the strict criterion, where only those 10-minute periods are accepted where the %Error \leq 15%, whereas the relaxed criterion allows periods with the %Error \leq 30%.

As mentioned earlier, an appropriate value of σ is needed to account for the LOS filtering by the lidar. Here we used a value of $\sigma = 9.5$ m (FWHM \approx 22.3 m) based on the amount of bias or average systematic error obtained after fitting the modeled structure function in (6) using a range of σ values between 7 m and 12 m with a step of 0.1 m. A value of $\sigma = 9.5$ m produced the least amount of bias in the ε estimation at all three heights (see Fig. 4) and therefore used in the analysis presented hereafter.

An illustration of estimating ε from sonic and lidar data is shown in Fig. 5. For both sonic anemometers and lidar, ε is calculated for those 10-minute time periods where $\overline{U} \ge 4 \text{ ms}^{-1}$ and the wind direction $\in [0^{\circ}-120^{\circ}]$ or $[225^{\circ}-360^{\circ}]$. The winds coming from the south sector $[121^{\circ}-224^{\circ}]$ were discarded to avoid wake flow from wind turbines at the test site and the wake from the mast itself. This study includes ε results from three heights: 103 m, 175 m, and 241 m. Results from the height of 37 m are excluded from the analysis because the pulsed lidar is blind for the heights below 30 m, and there are not enough data points to get a realistic second-order structure function.

5 Results and discussion

The atmospheric conditions observed at the Østerild test site during the lidar measurement period were predominantly neutral, with about 55% of the data falling in either of these three categories: nns, n, nnu. Stable atmospheric conditions (s, vs) occurred about 30% of the measurement time, while the unstable conditions (u, vu) were present for about only 15% of the time. With this in mind, let's view the $D_{\text{lidar}}(r)$ model fitting error, described in (12), as a function of the atmospheric stability in Fig. 6 at





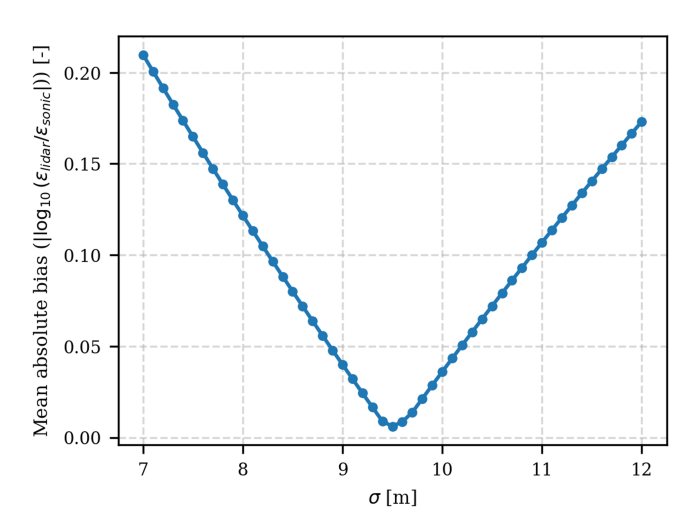


Figure 4. Mean bias or systematic error produced by fitting the modeled structure function over a range of σ values from 7 m to 12 m with a step of 0.1 m

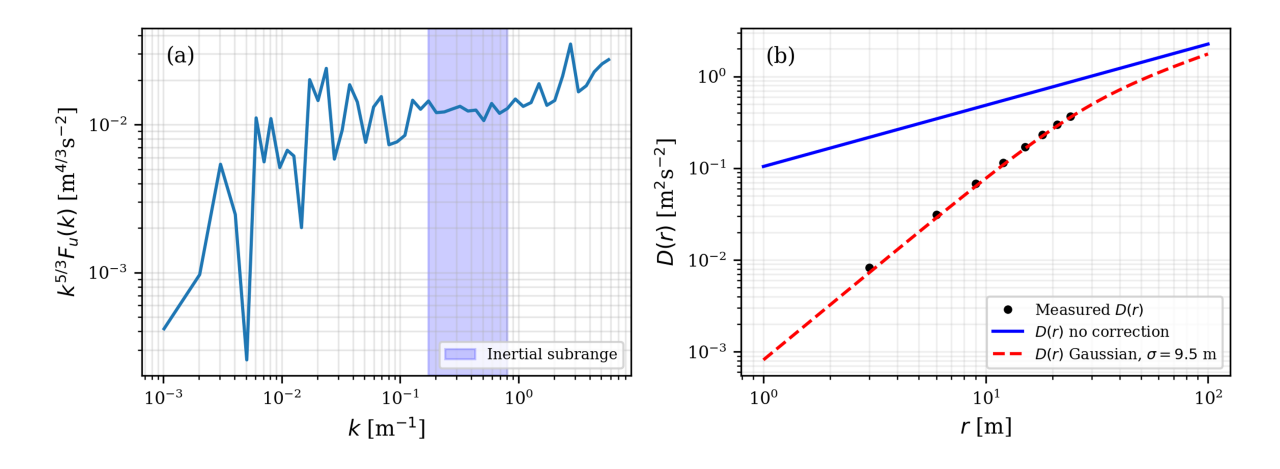


Figure 5. Two different ways used in this study to get turbulence energy dissipation rate ε . (a) Sonic anemometer: an illustration of the compensated spectrum $k_1^{5/3} \cdot F_u(k_1)$ and the inertial subrange at 103 m above ground level. (b) BEAM 6x lidar: an example of the measured structure function (black markers) and the D_{lidar} model in Eq. 6 fitted over it (red dashed line). The unfiltered D(r) with Kolmogorov's scaling of $r^{2/3}$ is also shown (blue line)



225

230



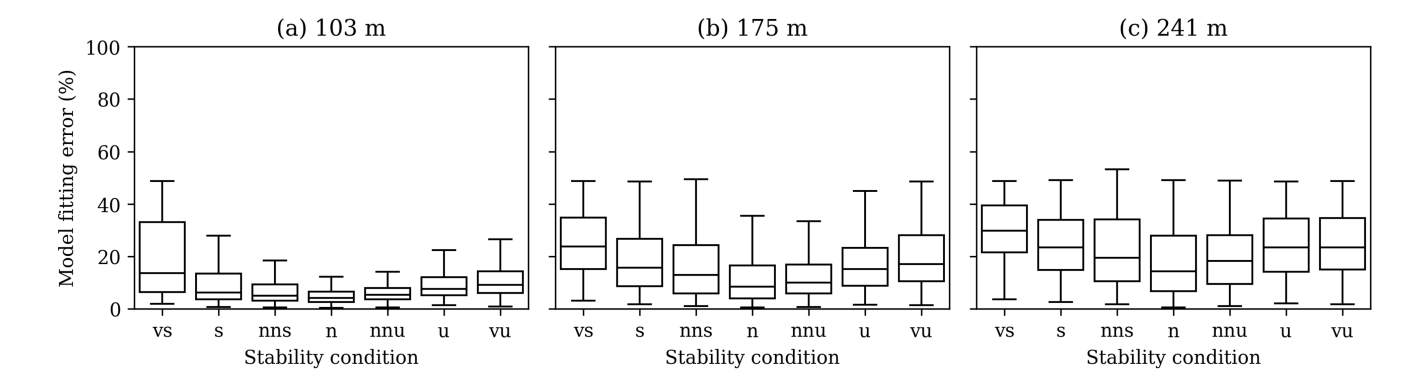


Figure 6. The model fitting error as a function of the seven stability classes described in Table 1 at three different heights: (a) 103 m, (b) 175 m, and (c) 241 m. The box plot shows the median (center line) and the first and third quartiles. The whiskers represent the minimum and maximum values of the observed error.

the three measurement heights of 103 m, 175 m, and 241 m. The neutral conditions (nns, n, nnu) produced the lowest fitting errors at all three heights. The unstable conditions (u and vu) showed slightly higher errors when fitting the structure function model over the measured data. The highest model fitting errors were observed for the very stable (vs) atmospheric conditions, as these conditions have the least amount of atmospheric turbulence, which makes it difficult to identify the inertial subrange. We also observed an increase in fitting errors with the increase in height, as both the median and maximum values of the errors were highest at 241 m for all stability conditions.

The comparison of turbulence energy dissipation rates obtained from lidar and sonic anemometers at the three heights of 103 m, 175 m, and 241 m is displayed in Fig. 7 and Fig. 8 for the strict and relaxed error criteria, respectively. The data shown here represents all seven stability classes and, therefore, is not subdivided. The number of available 10-minute time periods (N) that qualify for all the requirements, i.e., wind speed, wind direction, and whether the fitting error is within the defined limit, is highest at 103 m. The sample number subsequently drops for the higher heights because of the increase in the model fitting error and the difficulty in detecting the inertial subrange at higher heights. The point density plots show an excellent correlation between the two instruments for both criteria. For the strict criterion (\leq 15% error), a Pearson correlation coefficient (ρ) value of 0.96 at 103 m and 175 m, and 0.91 at 241 m was observed. For the relaxed criterion (\leq 30% error), the number of available 10-minute periods is increased significantly: from 90% of the available data to almost 100% at 103 m, from 60% of the available data to 85% at 175 m, and from 40% of the available data to 70% at 241 m. This increase is marked by a very slight decrease in ρ values: 0.94 at 103 m, 0.93 at 175 m, and 0.9 at 241 m. This implies that relaxing the error criterion significantly increases the amount of available data but does not severely sacrifice the correlation between lidar and sonic ε . Although the number of 10-minute periods where lidar overestimates ε increases, they are still relatively smaller in number, as indicated by the color in the density plots (see Fig. 8).

The bias analysis of the lidar obtained turbulence energy dissipation rates is presented in Fig. 9 and 10. Histograms of the $\log_{10}(\varepsilon_{\text{lidar}}/\varepsilon_{\text{sonic}})$ are illustrated in Fig. 9 for the three heights while the bias ranges of $\varepsilon_{\text{lidar}}$ relative to $\varepsilon_{\text{sonic}}$ are shown in Fig.





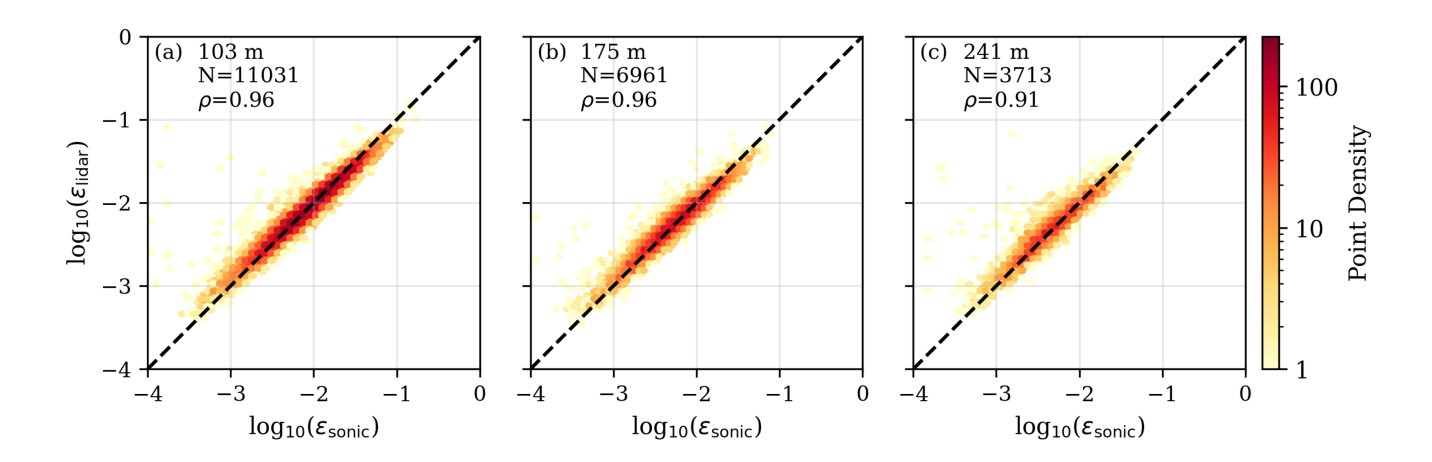


Figure 7. Comparison of $\varepsilon_{\text{lidar}}$ with $\varepsilon_{\text{sonic}}$ at three heights of (a) 103 m, (b) 175 m, and (c) 241 m for the strict criterion (model fitting error \leq 15%). The values are plotted on a log-log plot, and the black dashed line represents 1:1 correspondence. The number of 10-minute samples used in the plots (N) and the Pearson correlation coefficient (ρ) are also mentioned.

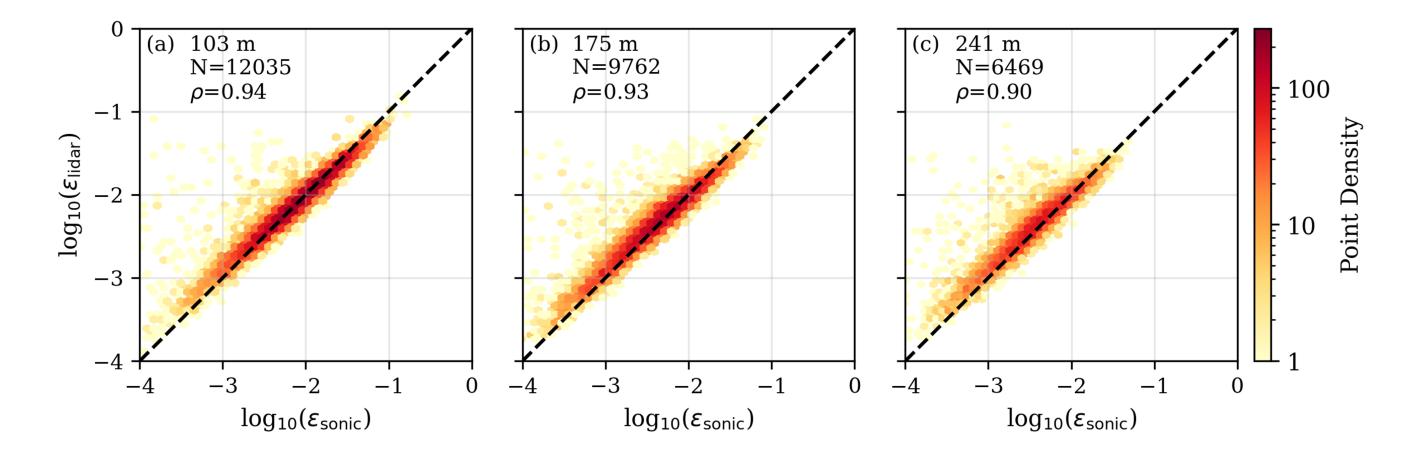


Figure 8. Same as Fig. 7 but for the relaxed error criterion (model fitting error $\leq 30\%$).



240

245

250



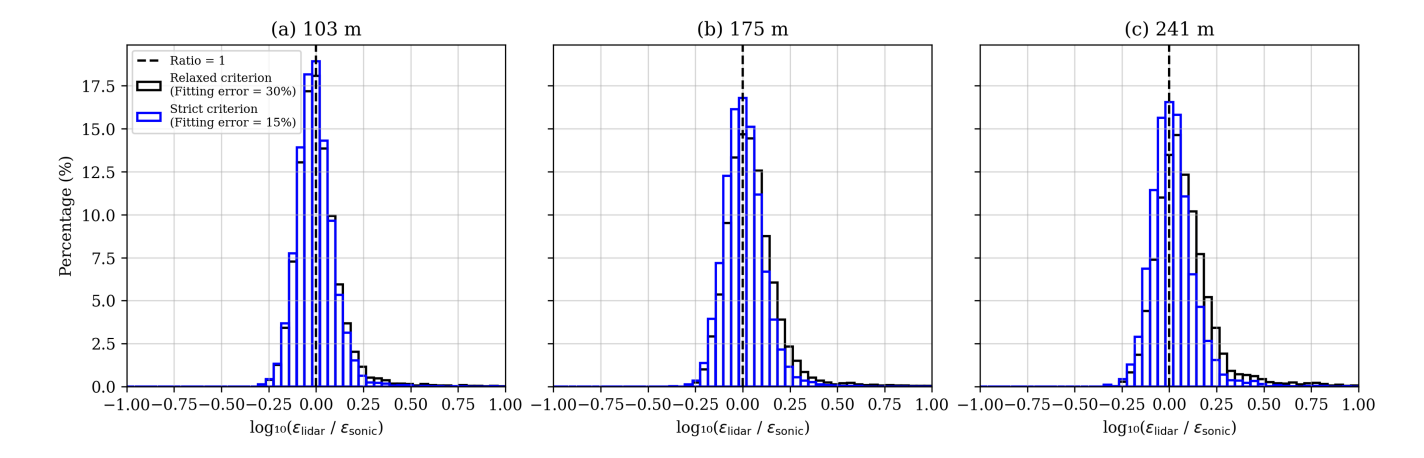


Figure 9. Histogram of $\log_{10}(\varepsilon_{\text{lidar}}/\varepsilon_{\text{sonic}})$ at the three heights under investigation, i.e, (a) 103 m, (b) 175 m, and (c) 241 m. Histograms are presented for both relaxed fitting criterion (in black color) and strict fitting criterion (in blue color).

10. These plots are shown for both relaxed and strict error criteria. From the histogram plots, one can see that the majority of data is centered around $\log_{10}(\varepsilon_{\text{lidar}}/\varepsilon_{\text{sonic}}) = 0$. For the strict criterion, there is no tail in the distribution on either side of the center. But for the relaxed criterion, a small tail on the right side, i.e. $\log_{10}(\varepsilon_{\text{lidar}}/\varepsilon_{\text{sonic}}) > 0$ is observed, which shows those 10-minute periods where the lidar overestimates ε . Combined, these data points represent less than 5% of the total data analyzed.

Another interesting way to look at the bias is to categorize the data in bias ranges, as seen in Fig. 10. For all three heights, more than 50% of the lidar obtained $\varepsilon_{\text{lidar}}$ values are within $\pm 20\%$ range of the $\varepsilon_{\text{sonic}}$. Similarly, >90% and >75% of $\varepsilon_{\text{lidar}}$ values obtained are inside the $\pm 40\%$ range of the $\varepsilon_{\text{sonic}}$ for the strict and relaxed error criteria, respectively. These results clearly show the high accuracy of the structure function method in obtaining the turbulence energy dissipation rate from a lidar possessing a high resolution of range gates.

The utility of the modeled structure function containing the lidar filtering effect in estimating ε is clearly observed in the above shown comparison. The largest source of random errors in this method originates from the detection of the inertial subrange. It was challenging to detect an inertial subrange during very stable atmospheric conditions and during low wind speeds (< 5 ms⁻¹) due to the lidar's filtering of small-scale turbulence structures. Since we used only the high-level lidar data, i.e., LOS velocities, in estimating ε , any fluctuation smaller than the lidar's probe volume length is going to be filtered out. A way to overcome this is to use the low-level lidar data, i.e., Doppler spectrum width, or to increase the range-gate resolution of the lidar beams. A comparison between the Doppler spectrum width (DSW) and the structure function methods is not performed here but kept for future investigation.

Unlike older systems, in modern lidar systems such as the one used in this study, instrument noise can be neglected (Mann et al., 2009; Sathe and Mann, 2013). Since the magnitude of ε spans the order of multiple decades (10^{-4} to 10^{-1}), the instrument noise can possibly pollute the measurements, especially at low ε values. However, the random errors from the





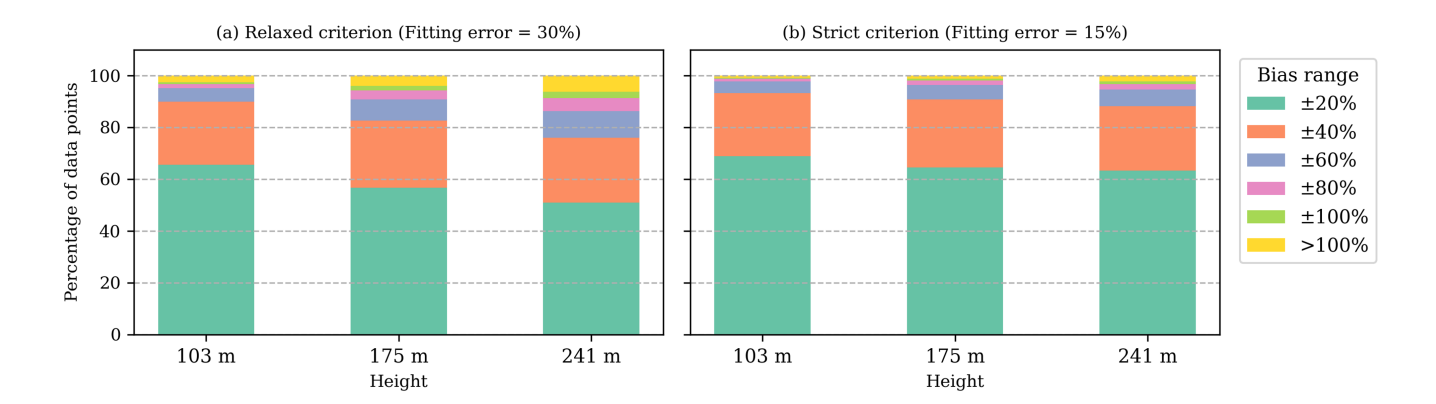


Figure 10. Bias ranges of $\varepsilon_{\text{lidar}}$ relative to $\varepsilon_{\text{sonic}}$. More than 60% of the lidar obtained turbulence energy dissipation rate values lie within $\pm 20\%$ of the values derived from sonic anemometers.

instrument noise are reduced by using a conservative threshold for the lidar *Intensity* parameter. A lower threshold would allow more data points at the cost of increasing the random error. Furthermore, the statistical uncertainty associated with the lidar-measured ε is reduced by taking the mean structure function for all six beams within the 10-minute time period and then fitting the model on that averaged measured structure function.

The excellent correlation between ε obtained from the lidar and sonic anemometer indicates that ε can be computed directly from the inertial subrange, provided that $\sigma < \mathcal{L}_o$. This also requires that the inertial subrange is detected with a high certainty, where the high range-gate resolution of the Beam 6x lidar proves especially useful. Large model fitting errors observed in the very stable atmospheric conditions (see Fig. 6), may indicate that the inertial subrange may not be detected properly or that the turbulence length scales are relatively small, i.e. $\mathcal{L}_o < \sigma$. A possible simple solution would be to include a correction parameter for very stable conditions in the structure function model or use a lidar with even higher range gate resolution. Recently introduced *Halo Photonics by Lumibird BEAM 6x Wind Power* lidar with a range gate resolution of 1.5 m along the beam can be used to resolve small-scale turbulence even further, but has not been tested yet.

6 Conclusions

255

260

265

270

A second-order longitudinal structure function model for lidar LOS velocities is presented in this article. The model also contains a Gaussian filter function to account for the probe volume averaging inside a pulsed lidar beam. The model is used to measure ε at three heights of 103 m, 175 m, and 241 m, with a six-beam pulsed lidar. The lidar obtained ε values were compared against ultrasonic anemometers.

The second-order structure function model presented here can be successfully used to estimate ε with a standalone lidar having a high range gate resolution. The lidar used here has a range gate resolution of 3 m and is able to effectively detect the inertial subrange. We compared almost 8 months of lidar-measured ε with the corresponding sonic-measured ε and found an excellent correlation between the two datasets. We observed Pearson correlation coefficient (ρ) values of more than 0.9 at all



285



three heights, significantly higher than similar previous studies, and methods (Smalikho and Banakh, 2017; Wildmann et al., 2020; Bodini et al., 2018). The observed bias was also very small, i.e., more than 50% of all the lidar-measured ε values lie within $\pm 20\%$ of the sonic-measured values.

It was observed that the main source of random errors in lidar-measured ε values is the improper detection of the inertial subrange. Since the structure function method heavily relies on the detection of the inertial subrange, relaxing the error criterion during model fitting can significantly increase random errors in the estimated ε . It is therefore advised to be cautious when using this method during low wind speed conditions (< 5 ms⁻¹), where lower atmospheric turbulence may result in possible contamination from instrument noise. During very stable atmospheric conditions, detecting the inertial subrange becomes even more challenging due to the smaller turbulence length scales, which are filtered by the lidar's probe volume averaging process. Prospective studies may include quantifying the random error originating from the instrumental noise, and a comparison with other similar methods, such as the Doppler spectrum width method to estimate ε . Additionally, the effect of lidar motion on ε measurements in a floating configuration, which we expect to be null, would also be an interesting investigation.

Appendix A: Derivation of lidar longitudinal structure function

It is convenient to transform the square of the integral in (5) to a double integral such that the ensemble average can be moved inside the integrals:

$$D_{\text{lidar}}(r) = \iint_{-\infty}^{\infty} \left\langle \left\{ v(x+s_1) - v(x+r+s_1) \right\} \left\{ v(x+s_2) - v(x+r+s_2) \right\} \right\rangle \varphi(s_1) \varphi(s_2) ds_1 ds_2 . \tag{A1}$$

Expanding the parentheses and using the definition of the covariance function $R(r) \equiv \langle v(x)v(x+r)\rangle$, the product of the curly parentheses can be written as

$$2R(s_1 - s_2) - R(s_1 - s_2 - r) - R(s_1 - s_2 + r) , (A2)$$

and if we further exploit the fact that due to the symmetry of φ the integrals over the last two terms are the same, and the formal relation D(r) = 2(R(0) - R(r)), the term can be written as

$$D(s_1 - s_2 - r) - D(s_1 - s_2)$$
 (A3)

We now transform the integration variables into $s=s_1-s_2$ and $s'=s_1+s_2$ with the Jacobian determinant $|\partial(ss')/\partial(s_1s_2)|=2$ such that

$$D_{\text{lidar}}(r) = \int_{-\infty}^{\infty} \left\{ D(s-r) - D(s) \right\} \int_{-\infty}^{\infty} \frac{1}{2} \varphi\left(\frac{s+s'}{2}\right) \varphi\left(\frac{s'-s}{2}\right) ds' ds . \tag{A4}$$

300 The inner integral over s' is essentially a convolution of two Gaussian functions, so the expression becomes

$$D_{\text{lidar}}(r) = \int_{-\infty}^{\infty} \left\{ D(s-r) - D(s) \right\} \frac{1}{2\sqrt{\pi}\sigma} \exp\left(-\frac{s^2}{4\sigma^2}\right) ds . \tag{A5}$$





Using the inertial subrange expression of the structure function (2) and consulting the symbolic algebra capabilities of *Mathematica*, we finally arrive at (6).

Author contributions. AHS conceptualized the work presented here. JM and AHS developed the model presented in this study. AHS and
 MM performed the data analysis. AHS wrote the initial draft of the manuscript. All authors reviewed and edited the manuscript. JM acquired the funding and resources for the work.

Competing interests. MM is employed by Lumibird SA, the manufacturer of the lidar used in this study. The other authors declare no competing interests.

Acknowledgements. The funding for JM and AHS comes from Atmospheric Flow, Loads and pOwer for Wind energy (FLOW, HORIZON-310 CL5-2021-D3-03-04, Grant number 101084205), funded by the European Union. MM's work is funded by HORIZON-MSCA-2022-DN-01 under grant agreement no. 101119550 (AptWind). The authors acknowledge the technical staff at DTU Wind Energy for maintaining the BEAM 6x lidars stationed at the Østerild test site. Special thanks to Alfredo Peña for valuable inputs and suggestions.





References

- Banakh, V. and Smalikho, I.: Determination of the turbulent energy dissipation rate from lidar sensing data, Atmospheric and oceanic optics c/c of optika atmosfery i okeana, 10, 295–302, 1997.
 - Bodini, N., Lundquist, J. K., and Newsom, R. K.: Estimation of turbulence dissipation rate and its variability from sonic anemometer and wind Doppler lidar during the XPIA field campaign, Atmospheric Measurement Techniques, 11, 4291–4308, https://doi.org/10.5194/amt-11-4291-2018, 2018.
- Bonin, T. A., Choukulkar, A., Brewer, W. A., Sandberg, S. P., Weickmann, A. M., Pichugina, Y. L., Banta, R. M., Oncley, S. P., and Wolfe,

 D. E.: Evaluation of turbulence measurement techniques from a single Doppler lidar, Atmospheric Measurement Techniques, 10, 3021–3039, https://doi.org/10.5194/amt-10-3021-2017, 2017.
 - Davis, J. C., Collier, C. G., Davies, F., and Bozier, K. E.: Spatial variations of sensible heat flux over an urban area measured using Doppler lidar, Meteorological Applications, 15, 367–380, https://doi.org/10.1002/met.79, 2008.
- Dolfi-Bouteyre, A., Canat, G., Lombard, L., Valla, M., Durécu, A., and Besson, C.: Long-range wind monitoring in real time with optimized coherent lidar, Optical Engineering, 56, 031 217–031 217, 2017.
 - Drobinski, P., Dabas, A. M., and Flamant, P. H.: Remote Measurement of Turbulent Wind Spectra by Heterodyne DopplerLidar Technique, Journal of Applied Meteorology, 39, 2434 2451, https://doi.org/10.1175/1520-0450(2000)039<2434:RMOTWS>2.0.CO;2, 2000.
 - Eberhard, W. L., Cupp, R. E., and Healy, K. R.: Doppler lidar measurement of profiles of turbulence and momentum flux, Journal of Atmospheric and Oceanic Technology, 6, 809–819, 1989.
- Frehlich, R. and Cornman, L.: Estimating spatial velocity statistics with coherent Doppler lidar, Journal of Atmospheric and Oceanic Technology, 19, 355–366, 2002.
 - Frehlich, R., Hannon, S. M., and Henderson, S. W.: Coherent Doppler lidar measurements of wind field statistics, Boundary-Layer Meteorology, 86, 233–256, 1998.
- Held, D. P. and Mann, J.: Comparison of methods to derive radial wind speed from a continuous-wave coherent lidar Doppler spectrum,

 Atmospheric Measurement Techniques, 11, 6339–6350, https://doi.org/10.5194/amt-11-6339-2018, 2018.
 - Kaimal, J. C. and Finnigan, J. J.: Atmospheric boundary layer flows: their structure and measurement, Oxford university press, 1994.
 - Liu, H., Shah, S. L., and Jiang, W.: On-line outlier detection and data cleaning, Comput. Chem. Eng., 28, 1635–1647, https://api. semanticscholar.org/CorpusID:15696230, 2004.
 - Mann, J.: The spatial structure of neutral atmospheric surface-layer turbulence, Journal of fluid mechanics, 273, 141-168, 1994.
- Mann, J., Cariou, J.-P. C., Parmentier, R. M., Wagner, R., Lindelöw, P., Sjöholm, M., and Enevoldsen, K.: Comparison of 3D turbulence measurements using three staring wind lidars and a sonic anemometer, Meteorologische Zeitschrift, 18, 135–140, https://doi.org/10.1127/0941-2948/2009/0370, 2009.
- O'Connor, E. J., Illingworth, A. J., Brooks, I. M., Westbrook, C. D., Hogan, R. J., Davies, F., and Brooks, B. J.: A Method for Estimating the Turbulent Kinetic Energy Dissipation Rate from a Vertically Pointing Doppler Lidar, and Independent Evaluation from Balloon-Borne
 In Situ Measurements, Journal of Atmospheric and Oceanic Technology, 27, 1652 1664, https://doi.org/10.1175/2010JTECHA1455.1, 2010.
 - Peña, A., Dellwik, E., and Mann, J.: A method to assess the accuracy of sonic anemometer measurements, Atmospheric Measurement Techniques, 12, 237–252, https://doi.org/10.5194/amt-12-237-2019, 2019.



355



- Peña, A., Yankova, G. G., and Mallini, V.: On the lidar-turbulence paradox and possible countermeasures, Wind Energy Science, 10, 83–102, https://doi.org/10.5194/wes-10-83-2025, 2025.
 - Peña, A.: Østerild: A natural laboratory for atmospheric turbulence, Journal of Renewable and Sustainable Energy, 11, 063 302, https://doi.org/10.1063/1.5121486, 2019.
 - Pope, S. B.: Turbulent Flows, Cambridge University Press, 2000.
 - Sathe, A. and Mann, J.: A review of turbulence measurements using ground-based wind lidars, Atmospheric Measurement Techniques, 6, 3147–3167, https://doi.org/10.5194/amt-6-3147-2013, 2013.
 - Sathe, A., Mann, J., Vasiljevic, N., and Lea, G.: A six-beam method to measure turbulence statistics using ground-based wind lidars, Atmospheric Measurement Techniques, 8, 729–740, https://doi.org/10.5194/amt-8-729-2015, 2015.
 - Smalikho, I., Köpp, F., and Rahm, S.: Measurement of atmospheric turbulence by $2-\mu$ m Doppler lidar, Journal of Atmospheric and Oceanic Technology, 22, 1733–1747, 2005.
- Smalikho, I. N. and Banakh, V. A.: Measurements of wind turbulence parameters by a conically scanning coherent Doppler lidar in the atmospheric boundary layer, Atmospheric Measurement Techniques, 10, 4191–4208, https://doi.org/10.5194/amt-10-4191-2017, 2017.
 - Stull, R. B.: An Introduction to Boundary Layer Meteorology, vol. 13 of *Atmospheric and Oceanographic Sciences Library*, Kluwer Academic Publishers (Springer), Dordrecht, Boston, London, 1 edn., ISBN 978-90-277-2769-5 (softcover), 978-94-009-3027-8 (eBook), https://doi.org/10.1007/978-94-009-3027-8, 1988.
- Syed, A. H., Mann, J., Platis, A., and Bange, J.: Turbulence structures and entrainment length scales in large offshore wind farms, Wind Energy Science, 8, 125–139, https://doi.org/10.5194/wes-8-125-2023, 2023.
 - Taylor, G. I.: Statistical theory of turbulence-II, Proceedings of the Royal Society of London. Series A-Mathematical and Physical Sciences, 151, 444–454, 1935.
- Wildmann, N., Bodini, N., Lundquist, J. K., Bariteau, L., and Wagner, J.: Estimation of turbulence dissipation rate from Doppler wind lidars and in situ instrumentation for the Perdigão 2017 campaign, Atmospheric Measurement Techniques, 12, 6401–6423, https://doi.org/10.5194/amt-12-6401-2019, 2019.
 - Wildmann, N., Päschke, E., Roiger, A., and Mallaun, C.: Towards improved turbulence estimation with Doppler wind lidar velocity-azimuth display (VAD) scans, Atmospheric Measurement Techniques, 13, 4141–4158, https://doi.org/10.5194/amt-13-4141-2020, 2020.